Precision of InSAR Time Series Across Different Wavelengths: Effects of Random-Motion-Induced Temporal Decorrelation

Kunyi Chen and Cunren Liang

***Abstract*—Synthetic Aperture Radar (SAR) Interferometry (InSAR) has entered the multiband era with the launch of the new generation of long-wavelength SAR missions. A fundamental question concerns the precision of the displacement time series and velocities obtained by InSAR time-series analysis techniques across different wavelengths. In this work, we investigate this problem by accounting for temporal decorrelation of distributed targets induced by the random motion of scatterers within a SAR resolution cell. We begin with the decorrelation model in the presence of random motion and then present the Cramér–Rao Lower Bound (CRLB) for the displacement time series and velocity. We derive the variances of the displacement series and velocity produced by representative Small BAseline Subset (SBAS) and phase-linking algorithms. The results demonstrate that, considering random motion alone, a longer wavelength SAR system can achieve a higher precision in measuring displacement and velocity with time-series techniques. This conclusion is validated by both simulation experiments and real-data experiments using multiband data acquired by the TropiSCAT experiment.**

***Index Terms*—Synthetic Aperture Radar (SAR), interferometry (InSAR), L-band, random motion, temporal decorrelation, time series.**

I. Introduction

EARLY spaceborne Synthetic Aperture Radar (SAR) data were mainly acquired by satellite SAR missions operating at shorter wavelengths, such as X-band and C-band. We are now entering a golden age of L-band SAR with the launch and operation of a fleet of L-band missions, including ALOS-2 [1], LuTan-1 [2], ALOS-4 [3], and NISAR [4]. The L-band data archive will be further enriched by the planned ROSE-L mission. In addition to its L-band SAR, NISAR also carries an S-band SAR, albeit with a much lower duty cycle. Recently, P-band spaceborne SAR data have become available with the launch of the BIOMASS mission [5]. Owing to these missions, spaceborne SAR data are currently available across all major microwave bands (from X-band to P-band) allocated by the International Telecommunications Union (ITU) for active remote sensing. In the future, there will be at least highly abundant C-band and L-band SAR data. Accordingly, SAR Interferometry (InSAR) is ushering in a multiband era. Then, a fundamental question arises: how do InSAR uncertainties compare across different wavelengths?

The total uncertainty of the InSAR displacement measurements includes an expectation component and a standard deviation component. Apart from processing errors, the expectation component often arises from atmospheric refraction [6], [7], [8], [9], [10], [11], ground motions not of interest [12], [13], [14], surface and near-surface physical processes other than motions [15], [16], and DEM and orbit errors (for some satellites with larger orbit uncertainties). This leads to a bias in the measurement, and therefore compromises their accuracy. These signals and errors, except for ionospheric refraction and surface and near-surface physical processes other than motion, would equally affect the InSAR displacement measurement across all wavelengths. The displacement error due to ionospheric refraction is proportional to radar wavelength squared, but it can be well estimated by the range split-spectrum method [17] at L-band. For shorter wavelengths, operational implementation of the method still faces significant challenges from decorrelation noise and phase-unwrapping errors [18]. The surface and near-surface physical processes other than motions that contribute to an InSAR phase are mostly associated with the dynamics of water. It is still not well understood how these processes affect InSAR phase, but several studies have shown that their direct impacts on InSAR phase are not very significant [15], [16]. The most notable impact is on the InSAR closure phase [19], which has been proven to be nonnegligible in time-series analysis techniques involving spatial averaging [20].

The standard deviation component arises from decorrelation [21] for distributed targets and from clutter for point targets [22]. It leads to lower precision in InSAR displacement measurements. Point targets are relatively well addressed by the Permanent Scatterer (PS) technique [23]. Decorrelation of distributed targets is the most significant issue in measuring displacement with InSAR. Concluding directly from the phase-to-displacement relationship, the conventional view holds that InSAR measurements at longer wavelengths generally have lower sensitivity, and thus lower precision, than those at shorter wavelengths. However, this is not necessarily true if we examine the decorrelation sources. Temporal decorrelation is the primary decorrelation source in InSAR displacement measurement. Other decorrelation sources can be removed,

Received 12 January 2026; revised 20 May 2026; accepted 17 June 2026. Date of publication 23 June 2026; date of current version 24 August 2026. This work was supported by the National Natural Science Foundation of China under Grant 42274026. *(Corresponding author: Cunren Liang.)*

The authors are with the Institute of Remote Sensing and Geographic Information System, School of Earth and Space Sciences, Peking University, Beijing 100871, China (e-mail: cky2366531304@stu.pku.edu.cn; cunren.liang@pku.edu.cn).

Digital Object Identifier 10.1109/TGRS.2026.3706530

1558-0644 © 2026 IEEE. All rights reserved, including rights for text and data mining, and training of artificial intelligence and similar technologies. Personal use is permitted, but republication/redistribution requires IEEE permission.
See https://www.ieee.org/publications/rights/index.html for more information.

Authorized licensed use limited to: Peking University. Downloaded on August 25,2026 at 14:45:26 UTC from IEEE Xplore. Restrictions apply.

quantified, or even negelected. Some early studies primarily focused on a phenomenological comparison of total temporal decorrelation across different wavelengths [10], [24]. A major source of temporal decorrelation is the random motion of the elementary scatterers within a SAR resolution cell [21], [25], [26], [27], [28]. It is essential to compare the precision of displacement measurements obtained from InSAR time-series analysis of distributed targets across different wavelengths in the presence of random motion. The results can provide key insights into InSAR uncertainties across different wavelengths.

To date, InSAR time-series analysis techniques for distributed targets can be broadly classified into two classes: Small BAseline Subset (SBAS) [29] and phase-linking [30] methods. SBAS simply solves for the displacement series through least-squares or singular-value-decomposition inversion of multilooked interferograms. Phase linking aims to optimally estimate the phase series by exploiting the full covariance matrix of the SAR image stack. The accurate estimation of the covariance matrix in phase linking hinges on the identification of Statistically Homogeneous Pixels (SHPs) within the distributed target. There have been several phase-linking algorithms [31], [32], [33] since the method was first proposed [30]. Furthermore, in [34], a sequential phase-linking estimator, which partitions the original dataset into subsets, was developed to improve the computational efficiency. Some of these algorithms are now available in open-source software packages such as Mintpy [35] and Miaplpy [36].

In this work, we compare the precision of InSAR time-series displacement measurements across different wavelengths in the presence of random-motion-induced temporal decorrelation. This article is structured as follows. In Section II, after modeling the random-motion-induced temporal decorrelation across different wavelengths, we present the Cramér–Rao Lower Bound (CRLB) for the displacement series and velocity, and trace error propagation in the SBAS and phase-linking methods as implemented by representative algorithms. In Section III, we validate the derived theory through simulation experiments. In Section IV, we provide further evidence for the theory by processing real multiband data acquired by the TropiSCAT experiment. Finally, Section V concludes this article.

II. Theory

A. Overview of Repeat-Pass InSAR Decorrelation

A resolution cell of a SAR image is generally composed of a large number of scatterers, and its signal is the superposition of the signals from all scatterers. At time t, it can be represented by

$$S(t) = \sum_{n=1}^{N} s_n(t) \exp\left[-\mathrm{j}\frac{4\pi}{\lambda} R_n(t)\right] \tag{1}$$

where $s_n(t)$ represents the complex reflectivity of the nth scatterer at time t, λ is the radar wavelength, and $R_n(t)$ is the distance between the nth scatterer and the phase center of the radar antenna. If N is large enough, and no single scatterer's reflectivity is remarkably larger than the other scatterers' reflectivities, the random variable $S(t)$ follows a zero-mean complex circular Gaussian distribution. The complex coherence between the two random variables $S(t_1)$ and $S(t_2)$ acquired at times t_1 and t_2 can then be given by

$$\gamma^{\mathrm{c}}_{t_1,t_2} = \frac{\mathrm{E}\left[S(t_1)\, S(t_2)^*\right]}{\sqrt{\mathrm{E}\left[|S(t_1)|^2\right] \mathrm{E}\left[|S(t_2)|^2\right]}}. \tag{2}$$

The following analysis considers only its magnitude $\gamma_{t_1,t_2} = |\gamma^{\mathrm{c}}_{t_1,t_2}|$.

Considering different independent decorrelation sources, the coherence can be expressed as the product of thermal noise decorrelation, processing decorrelation, ambiguity decorrelation, geometry decorrelation, volume decorrelation, and temporal decorrelation

$$\gamma_{t_1,t_2} = \gamma_{\mathrm{thermal}} \cdot \gamma_{\mathrm{proc}} \cdot \gamma_{\mathrm{amb}} \cdot \gamma_{\mathrm{geo}} \cdot \gamma_{\mathrm{vol}} \cdot \gamma_{\mathrm{temp}}. \tag{3}$$

The first three decorrelation effects depend exclusively on radar system parameters and processing errors. Thermal noise decorrelation mainly arises from the random thermal motion of electrons within the hardware components and the thermal radiation received by the antenna from the environment. It can be quantified by the thermal Signal-to-Noise Ratio (SNR) as [21], [37]

$$\gamma_{\mathrm{thermal}} = \frac{1}{\sqrt{\left(1 + \mathrm{SNR}_{t_1}^{-1}\right)\left(1 + \mathrm{SNR}_{t_2}^{-1}\right)}}. \tag{4}$$

Processing decorrelation mainly results from the quantization errors [37], approximations involved in matched filtering, and coregistration errors [38]. Among them, the quantization effects can be approximated as additive white Gaussian noise [37]. Coregistration decorrelation can be quantified by [38]

$$\gamma_{\mathrm{coreg}} = \begin{cases} \mathrm{sinc}(\mu) = \dfrac{\sin(\pi\mu)}{\pi\mu}, & 0 \le \mu \le 1 \\ 0, & \mu > 1 \end{cases} \tag{5}$$

where the relative shift μ represents a fraction of the range (or azimuth) resolution cell. Ambiguity decorrelation is related to the pulse repetition frequency and the echo receiving window of the radar system. It can be calculated as [37]

$$\gamma_{\mathrm{amb}} = \frac{1}{1 + \mathrm{RASR}} \cdot \frac{1}{1 + \mathrm{AASR}} \tag{6}$$

where RASR is the range ambiguity-to-signal ratio, and AASR is the azimuth ambiguity-to-signal ratio. Therefore, all these three effects can be quantified [39], and the resulting precision loss of the InSAR measurements across different wavelengths can be easily evaluated.

Geometry decorrelation represents the loss of coherence caused by nonoverlapping spectra due to different observation geometries in both the range [40] and azimuth directions. It can be simply quantified as [38]

$$\gamma_{\mathrm{geo}} = \gamma_{\mathrm{rg}} \cdot \gamma_{\mathrm{az}} = \left(1 - \frac{|\Delta f_{\mathrm{WS}}|}{B_{\mathrm{rg}}}\right) \cdot \left(1 - \frac{|\Delta f_{\mathrm{DC}}|}{B_{\mathrm{az}}}\right) \tag{7}$$

where B_{az} and B_{rg} are the range and azimuth bandwidths, Δf_{DC} is the Doppler centroid frequency difference between the two observations, and Δf_{WS} is the range spectral shift caused by a nonzero perpendicular baseline. Geometry decorrelation can

Authorized licensed use limited to: Peking University. Downloaded on August 25,2026 at 14:45:26 UTC from IEEE Xplore. Restrictions apply.

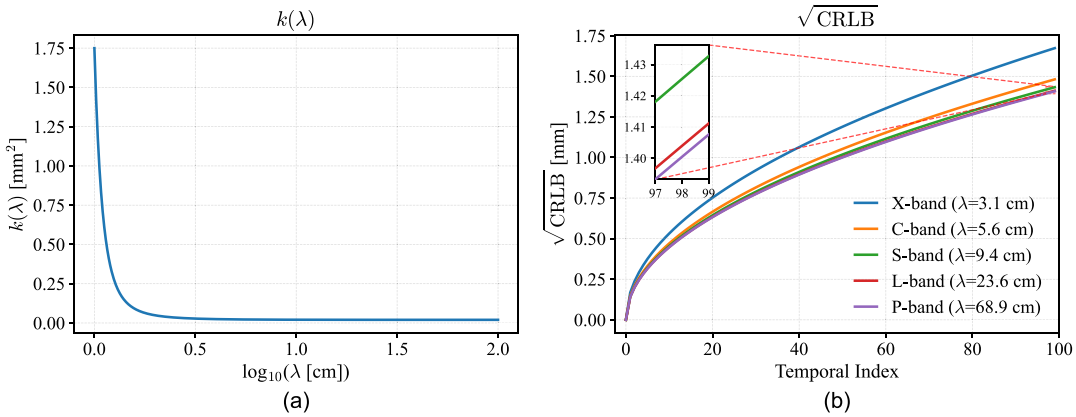

Fig. 1. (a) Variation of $k(\lambda)$ with λ. (b) CRLB of the displacement series for 100 acquisitions. The first acquisition is taken as the reference. Here, σ = 2.0 mm and the number of looks is 100. A logarithmic scale is used in (a) on the horizontal axis for clarity.

be removed by bandpass filtering. Even if the implementation of the required range bandpass filtering is challenging, the resulting precision loss of the InSAR measurements across different wavelengths can be easily evaluated.

Volume decorrelation is a combined effect of volume scattering and a nonzero perpendicular baseline. It occurs where the radar signal penetrates the medium on the ground. Formulating this effect is challenging, as it would require knowledge of penetration depth, reflectivity, and wave extinction coefficient in the medium. Nevertheless, volume decorrelation is minimized by the small orbit tubes maintained by current satellites.

Temporal decorrelation is the most significant decorrelation source and normally dominates the total decorrelation and hence the precision in repeat-pass InSAR. Temporal decorrelation can arise from:

1) The random motions of the scatterers,
2) the changes in the dielectric properties of the scatterers, and
3) the addition or removal of the scatterers in the resolution cell.

Among them, random motion is recognized as a significant source of temporal decorrelation [21], [25], [26], [27], [28]. In Sections II-B–II-E, we will quantify and compare the impacts of random-motion-induced temporal decorrelation on the precision of InSAR time series across different wavelengths.

B. Modeling Random-Motion-Induced Temporal Decorrelation

Considering a single resolution cell, the expectation of the InSAR signal is given by

$$\mathrm{E}\left[S\left(t_1\right)S\left(t_2\right)^*\right]=\mathrm{E}\left[\left(\sum_{n=1}^{N}s_n\left(t_1\right)\exp\left[-\mathrm{j}\phi_n\left(t_1\right)\right]\right)\times\left(\sum_{n=1}^{N}s_n\left(t_2\right)^*\exp\left[\mathrm{j}\phi_n\left(t_2\right)\right]\right)\right] \tag{8}$$

where $\phi_n(t) = 4\pi R_n(t)/\lambda$. Under the first-order Born approximation, mutual interactions among the scatterers are negelected and hence, the scatterers are independent. Assuming the change of each scatterer is only a random motion with a magnitude of $\Delta R_n(t_1, t_2)$ in the Line-Of-Sight (LOS) direction, (8) can be simplified as follows

$$\mathrm{E}\left[S\left(t_1\right)S\left(t_2\right)^*\right]=\sum_{n=1}^{N}\mathrm{E}\left[s_n\left(t_1\right)s_n\left(t_2\right)^*\right]\mathrm{E}\left\{\exp\left[-\mathrm{j}\frac{4\pi}{\lambda}\Delta R_n\left(t_1,t_2\right)\right]\right\}. \tag{9}$$

Furthermore, assume that $\Delta R_n(t_1, t_2)$ of each scatterer follows the same Gaussian distribution with a variance proportional to the time interval between the two acquisitions, i.e., $\Delta R_n(t_1, t_2) = \Delta R(t_1, t_2) \sim N(0, |t_1 - t_2|\sigma_p^2)$. Then the coherence can be derived as follows

$$\gamma_{t_1,t_2}=\mathrm{E}\left[\exp\left(-\mathrm{j}\frac{4\pi}{\lambda}\Delta R_{t_1,t_2}\right)\right]=\exp\left(-\frac{8\pi^2\sigma_p^2}{\lambda^2}\left|t_1-t_2\right|\right). \tag{10}$$

For a stack of N repeat-pass SAR acquisitions, its coherence matrix $\mathbf{\Gamma}$ can be formulated. If we assume the time interval of every two neighboring acquisitions is the same, i.e., SAR acquires data on every pass in the study area, then the element of $\mathbf{\Gamma}$ at position (m, n) can be given by

$$\mathbf{\Gamma}_{m,n}=\exp\left(-\frac{8\pi^2\sigma^2}{\lambda^2}|m-n|\right) \tag{11}$$

where $\sigma^2 = \sigma_p^2 t_p$, t_p is the revisiting period, and $1 \le m, n \le N$. This matrix is an exponentially decaying Toeplitz matrix. The inverse matrix of $\mathbf{\Gamma}$ is tridiagonal and is found to be

$$\mathbf{\Gamma}^{-1}=\frac{1}{1-\gamma\left(\lambda\right)^2}\times\begin{bmatrix}1 & -\gamma\left(\lambda\right) & \cdots & 0 & 0\\ -\gamma\left(\lambda\right) & 1+\gamma\left(\lambda\right)^2 & \ddots & 0 & 0\\ 0 & -\gamma\left(\lambda\right) & \ddots & -\gamma\left(\lambda\right) & 0\\ \vdots & \ddots & \ddots & 1+\gamma\left(\lambda\right)^2 & -\gamma\left(\lambda\right)\\ 0 & 0 & \cdots & -\gamma\left(\lambda\right) & 1\end{bmatrix} \tag{12}$$

where

$$\gamma\left(\lambda\right)=\exp\left(-\frac{8\pi^2\sigma^2}{\lambda^2}\right). \tag{13}$$

Authorized licensed use limited to: Peking University. Downloaded on August 25,2026 at 14:45:26 UTC from IEEE Xplore. Restrictions apply.

TABLE I

STANDARD DEVIATIONS OF THE VELOCITIES OBTAINED BY SBAS FOR DIFFERENT WAVELENGTHS UNDER DIFFERENT WEIGHTING SCHEMES. 1) IDENTITY MATRIX. 2) INVERSE MATRIX OF DIAGONAL VARIANCE MATRIX. 3) INVERSE MATRIX OF COVARIANCE MATRIX. THE NETWORK IS FULLY CONNECTED BUT EXCLUDES PAIRS WITH A COHERENCE BELOW 0.25. HERE, T_P = 12/365.25 YEAR AND UNIT OF STANDARD DEVIATION: MM/YR

	Weighting Matrix in (27)	Weighting Matrix in (24) 1	2	3	$\sqrt{\text{CRLB}}$
X-band (3.1 cm)	1	0.73	0.65	0.56	0.51
	2	0.78	0.68	0.59	
	3	0.67	0.59	0.51	
C-band (5.6 cm)	1	0.70	0.61	0.50	0.46
	2	0.74	0.64	0.52	
	3	0.64	0.56	0.46	
S-band (9.4 cm)	1	0.70	0.61	0.48	0.44
	2	0.74	0.63	0.51	
	3	0.64	0.55	0.44	
L-band (23.6 cm)	1	0.54	0.52	0.47	0.43
	2	0.58	0.54	0.50	
	3	0.50	0.47	0.43	
P-band (68.9 cm)	1	0.48	0.48	0.47	0.43
	2	0.51	0.50	0.50	
	3	0.44	0.44	0.43	

TABLE II

STANDARD DEVIATIONS OF THE VELOCITIES OBTAINED BY SBAS FOR DIFFERENT WAVELENGTHS UNDER DIFFERENT WEIGHTING SCHEMES. 1) IDENTITY MATRIX. 2) INVERSE MATRIX OF DIAGONAL VARIANCE MATRIX. 3) INVERSE MATRIX OF COVARIANCE MATRIX. THE NETWORK IS FORMED BY CONNECTING SIX SUBSEQUENT ACQUISITIONS BUT EXCLUDES PAIRS WITH A COHERENCE BELOW 0.25. HERE, T_P = 12/365.25 YEAR AND UNIT OF STANDARD DEVIATION: MM/YR

	Weighting Matrix in (27)	Weighting Matrix in (24) 1	2	3	$\sqrt{\text{CRLB}}$
X-band (3.1 cm)	1	0.73	0.65	0.56	0.51
	2	0.78	0.68	0.59	
	3	0.67	0.59	0.51	
C-band (5.6 cm)	1	0.56	0.54	0.50	0.46
	2	0.59	0.57	0.52	
	3	0.51	0.50	0.46	
S-band (9.4 cm)	1	0.50	0.49	0.48	0.44
	2	0.53	0.52	0.51	
	3	0.46	0.45	0.44	
L-band (23.6 cm)	1	0.48	0.48	0.47	0.43
	2	0.50	0.50	0.50	
	3	0.44	0.44	0.43	
P-band (68.9 cm)	1	0.47	0.47	0.47	0.43
	2	0.50	0.50	0.50	
	3	0.43	0.43	0.43	

C. CRLB of Displacement Series and Velocity

The CRLB for the phase series is given by [41]

$$\text{CRLB}_{\boldsymbol{\varphi}} = \left(\boldsymbol{\Theta}^{\mathrm{T}}\mathbf{X}\boldsymbol{\Theta}\right)^{-1} \tag{14}$$

where $\boldsymbol{\Theta}$ is the Jacobian matrix of the phase series with respect to itself, and here, it is an identity matrix $\mathbf{I}$, and $\mathbf{X}$ is the Fisher information matrix (FIM)

$$\mathbf{X} = 2L\left(\boldsymbol{\Gamma}\circ\boldsymbol{\Gamma}^{-1} - \mathbf{I}\right) \tag{15}$$

where L is the number of looks, and $\circ$ represents the Hadamard product. Substituting (11) and (12) into (15), $\text{CRLB}_{\boldsymbol{\varphi}}(\lambda)$ becomes

$$\text{CRLB}_{\boldsymbol{\varphi}}(\lambda) = \frac{1-\gamma(\lambda)^2}{2L\gamma(\lambda)^2}\left(\boldsymbol{\Theta}^{\mathrm{T}}\mathbf{Y}\boldsymbol{\Theta}\right)^{-1} \tag{16}$$

where the matrix $\mathbf{Y}$ is independent of wavelength and is given by

$$\mathbf{Y} = \begin{bmatrix} 1 & -1 & 0 & \cdots & 0 \\ -1 & 2 & -1 & \ddots & \vdots \\ 0 & -1 & \ddots & \ddots & 0 \\ \vdots & \ddots & \ddots & 2 & -1 \\ 0 & \cdots & 0 & -1 & 1 \end{bmatrix}. \tag{17}$$

Substituting (13) into (16), the CRLB for the displacement series can be given by

$$\text{CRLB}_{\mathbf{D}}(\lambda) = k(\lambda)\cdot\left(\boldsymbol{\Theta}^{\mathrm{T}}\mathbf{Y}\boldsymbol{\Theta}\right)^{-1} \tag{18}$$

where

$$k(\lambda) = \frac{\lambda^2\left(e^{16\pi^2\sigma^2/\lambda^2} - 1\right)}{32\pi^2 L}. \tag{19}$$

The matrix $(\boldsymbol{\Theta}^{\mathrm{T}}\mathbf{Y}\boldsymbol{\Theta})^{-1}$ is independent of wavelength, and $k(\lambda)$ decreases as λ increases, as shown in Fig. 1(a). Therefore, the absolute value of each element within $\text{CRLB}_{\mathbf{D}}(\lambda)$ decreases as λ increases. The singularity of matrix $\mathbf{Y}$ precludes direct inversion. To address this problem, we can set the ith acquisition as the reference a priori, thereby defining $\mathbf{Y}$ as its submatrix with the ith row and ith column removed. Fig. 1(b) shows the standard deviation lower bound of the displacement series with the first acquisition as the reference. Note that in Fig. 1, we have set $N = 100$ acquisitions, $\sigma = 2.0$ mm, and $L = 100$ looks. The number of looks is large, leading to very small standard deviations of the displacement series and velocity. These settings are used throughout this article.

For velocity, we assume a simple linear displacement with respect to time, i.e.,

$$D_n = -\frac{\lambda}{4\pi}\varphi_n = D_1 + v\cdot(n-1)\,t_p \tag{20}$$

Authorized licensed use limited to: Peking University. Downloaded on August 25,2026 at 14:45:26 UTC from IEEE Xplore. Restrictions apply.

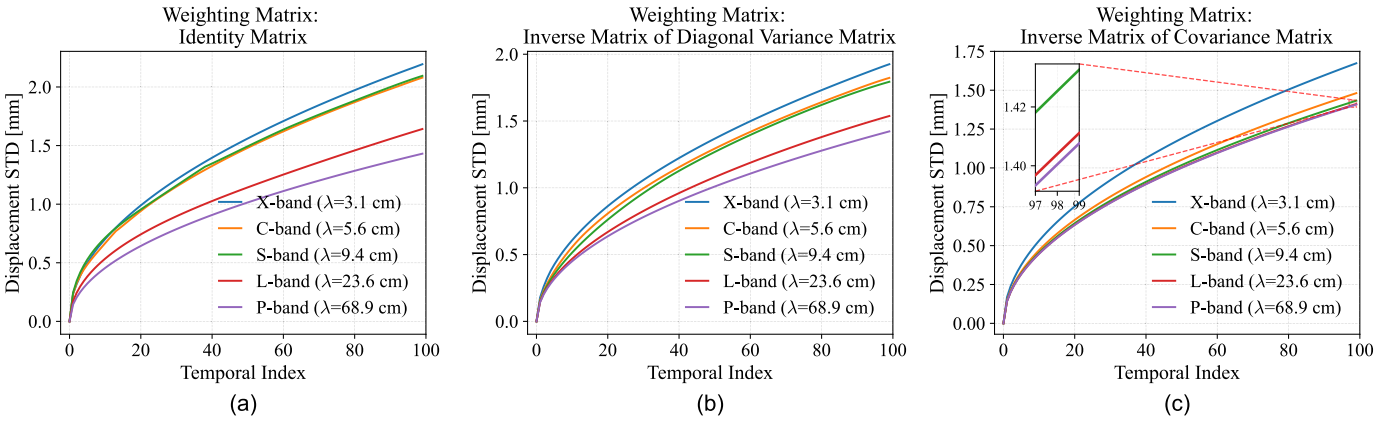

Fig. 2. Standard deviations of the displacement series obtained by SBAS for different wavelengths under three weighting schemes in (24). (a) Identity matrix, (b) inverse matrix of the diagonal variance matrix, and (c) inverse matrix of the covariance matrix. The network is fully connected but excluding pairs with a coherence below 0.25. The first acquisition is taken as the reference. Here, $\sigma = 2.0$ mm and the number of looks is 100.

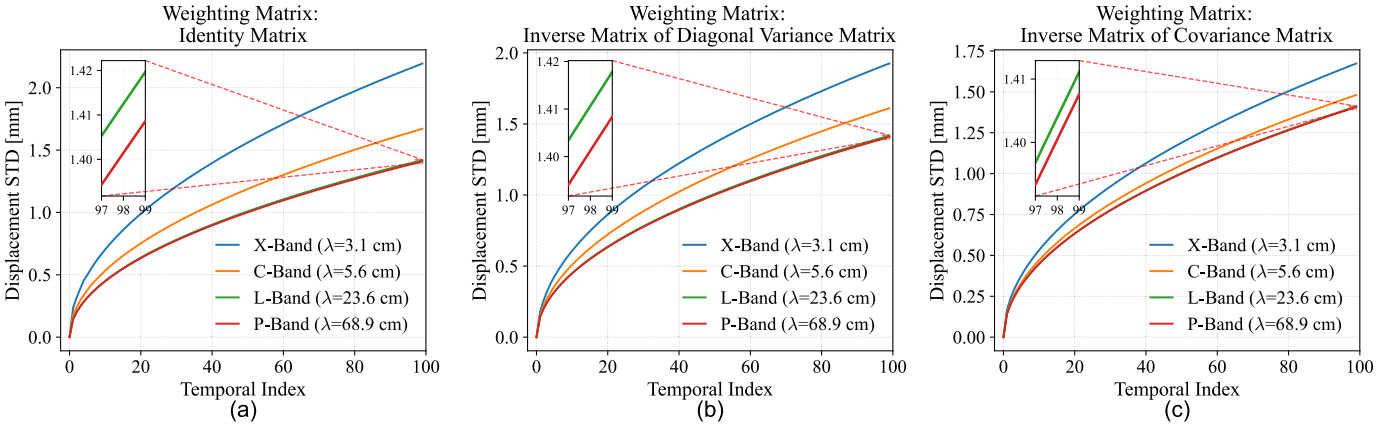

Fig. 3. Standard deviations of the displacement series obtained by SBAS for different wavelengths under three weighting schemes in (24). (a) Identity matrix, (b) inverse matrix of the diagonal variance matrix, and (c) inverse matrix of the covariance matrix. The network is formed by connecting six subsequent acquisitions but excluding pairs with a coherence below 0.25. The first acquisition is taken as the reference. Here, $\sigma = 2.0$ mm and the number of looks is 100.

where v is the displacement velocity in the LOS direction, and D_1 is the displacement of the first acquisition. Here, $\boldsymbol{\Theta}$ becomes the differential matrix of the phase series with respect to D_1 and v, i.e.,

$$\boldsymbol{\Theta}^{\mathrm{T}} = -\frac{4\pi}{\lambda} \cdot \begin{bmatrix} 1 & 1 & 1 & \cdots & 1 \\ 0 & t_p & 2t_p & \cdots & (N-1)\,t_p \end{bmatrix}. \tag{21}$$

Then the CRLB of the velocity can be derived as

$$\mathrm{CRLB}_v(\lambda) = \frac{k(\lambda)}{(N-1)\,t_p^2}. \tag{22}$$

Again, $\mathrm{CRLB}_v(\lambda)$ decreases as λ increases. These results imply that, considering only random-motion-induced temporal decorrelation, a SAR system with a longer wavelength can achieve higher precision in measuring both displacement and velocity using InSAR time-series techniques.

D. Error Propagation of SBAS

The SBAS technique generally refers to a class of algorithms used to invert the unwrapped interferometric phases to obtain the phase time series [29]. The most commonly used one is a least-squares estimation, i.e.,

$$\boldsymbol{\varphi}_{\mathrm{SBAS}} = \left(\mathbf{H}_{\boldsymbol{\phi}}^{\mathrm{T}}\mathbf{W}_{\boldsymbol{\phi}}\mathbf{H}_{\boldsymbol{\phi}}\right)^{-1}\mathbf{H}_{\boldsymbol{\phi}}^{\mathrm{T}}\mathbf{W}_{\boldsymbol{\phi}}\boldsymbol{\phi} \tag{23}$$

where $\mathbf{H}_{\boldsymbol{\phi}}$ is the observation matrix, $\mathbf{W}_{\boldsymbol{\phi}}$ is the weighting matrix, and $\boldsymbol{\phi}$ is the vector of unwrapped phases. The covariance matrix of the phase series is given by [42]

$$\mathbf{C}_{\boldsymbol{\varphi}_{\mathrm{SBAS}}} = \left(\mathbf{H}_{\boldsymbol{\phi}}^{\mathrm{T}}\mathbf{W}_{\boldsymbol{\phi}}\mathbf{H}_{\boldsymbol{\phi}}\right)^{-1}\mathbf{H}_{\boldsymbol{\phi}}^{\mathrm{T}}\mathbf{W}_{\boldsymbol{\phi}}\mathbf{C}_{\boldsymbol{\phi}}\mathbf{W}_{\boldsymbol{\phi}}\mathbf{H}_{\boldsymbol{\phi}}\left(\mathbf{H}_{\boldsymbol{\phi}}^{\mathrm{T}}\mathbf{W}_{\boldsymbol{\phi}}\mathbf{H}_{\boldsymbol{\phi}}\right)^{-1} \tag{24}$$

where $\mathbf{C}_{\boldsymbol{\phi}}$ is the covariance matrix of the interferometric phases. Accordingly, the covariance matrix of the displacement series is given by

$$\mathbf{C}_{\mathbf{D}_{\mathrm{SBAS}}} = \frac{\lambda^2}{16\pi^2}\mathbf{C}_{\boldsymbol{\varphi}_{\mathrm{SBAS}}}. \tag{25}$$

The mean velocity is also estimated through a least-squares inversion. According to (20), the observation matrix is given by

$$\mathbf{H}_{\mathbf{D}}^{\mathrm{T}} = \begin{bmatrix} 1 & 1 & 1 & \cdots & 1 \\ 0 & t_p & 2t_p & \cdots & (N-1)\,t_p \end{bmatrix}. \tag{26}$$

Authorized licensed use limited to: Peking University. Downloaded on August 25,2026 at 14:45:26 UTC from IEEE Xplore. Restrictions apply.

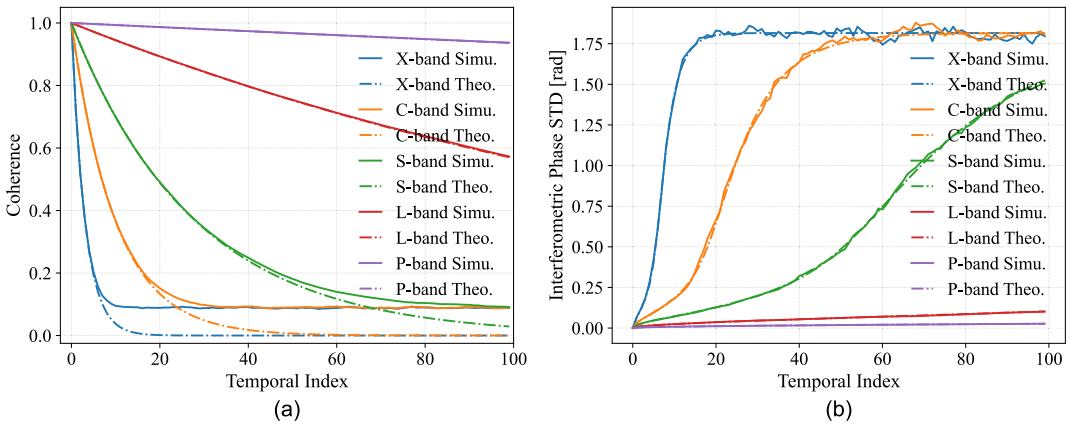

Fig. 4. Comparison between simulated and theoretical values of (a) coherence and (b) interferometric phase standard deviation between subsequent observations and the first acquisition. Here, $\sigma = 2.0$ mm and the number of looks is 100.

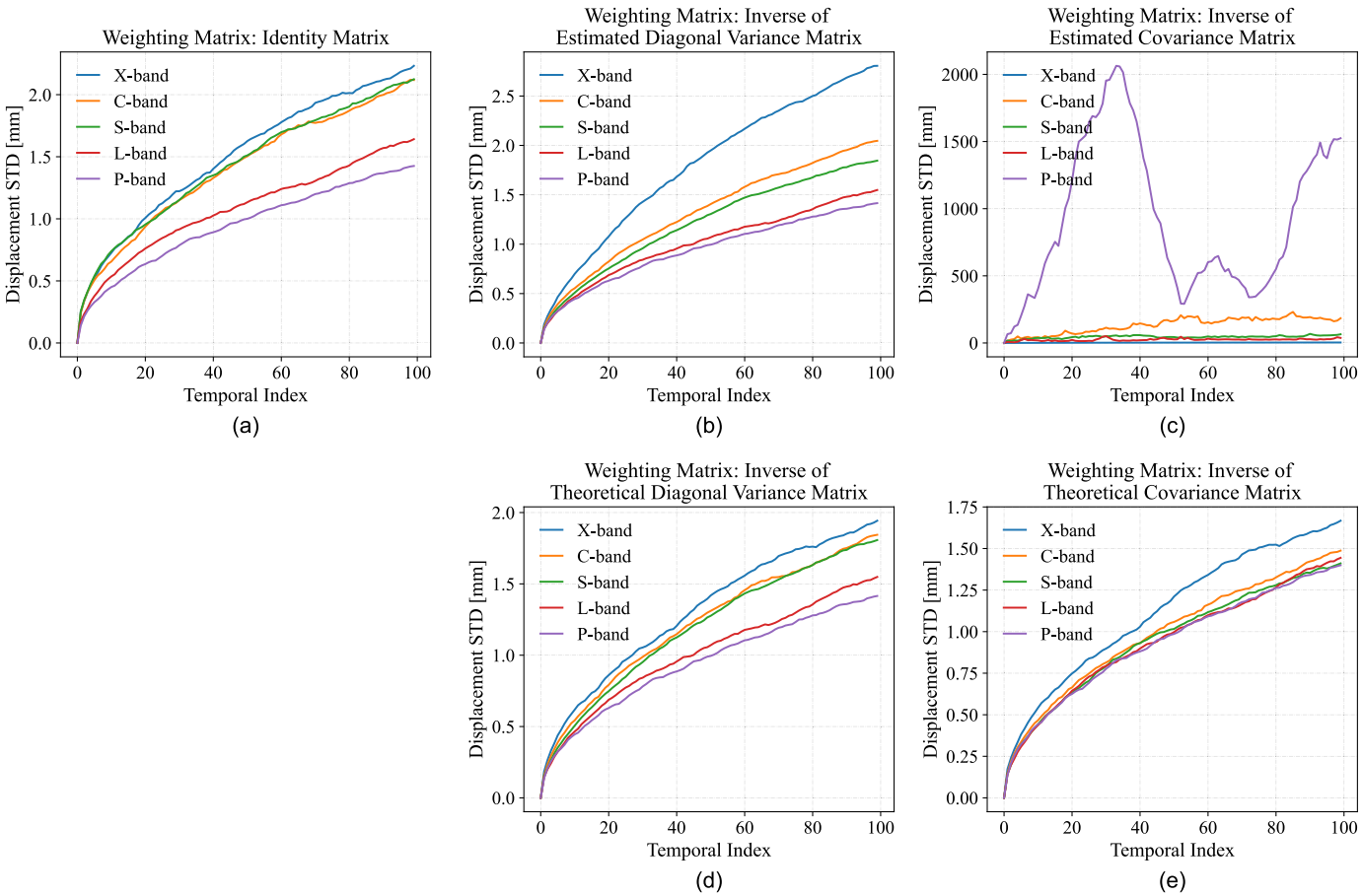

Fig. 5. Standard deviations of the displacement series obtained by SBAS for different wavelengths in simulation under two coherence schemes and three weighting schemes in (24). (a) Identity matrix, inverse matrix of the diagonal variance matrix calculated using (b) estimated coherence in simulation and (d) theoretical coherence, and inverse matrix of the covariance matrix calculated using (c) estimated coherence in simulation and (e) theoretical coherence. The network is fully connected but excludes pairs with a coherence below 0.25. The first acquisition is taken as the reference. Here, $\sigma = 2.0$ mm and the number of looks is 100.

Then the covariance matrix for the initial displacement D_1 and the mean velocity v can be derived as

$$\mathbf{C}_{\mathbf{V}_{\mathrm{SBAS}}} = \left(\mathbf{H}_{\mathbf{D}}^{\mathrm{T}}\mathbf{W}_{\mathbf{D}}\mathbf{H}_{\mathbf{D}}\right)^{-1}\mathbf{H}_{\mathbf{D}}^{\mathrm{T}}\mathbf{W}_{\mathbf{D}}\mathbf{C}_{\mathbf{D}_{\mathrm{SBAS}}}\mathbf{W}_{\mathbf{D}}\mathbf{H}_{\mathbf{D}}\left(\mathbf{H}_{\mathbf{D}}^{\mathrm{T}}\mathbf{W}_{\mathbf{D}}\mathbf{H}_{\mathbf{D}}\right)^{-1}. \tag{27}$$

The weighting matrix $\mathbf{W}_{\boldsymbol{\phi}}$ and $\mathbf{W}_{\mathbf{D}}$ can be calculated as the inverses of $\mathbf{C}_{\boldsymbol{\phi}}$ and $\mathbf{C}_{\boldsymbol{\varphi}_{\mathrm{SBAS}}}$, respectively.

To calculate $\mathbf{C}_{\mathbf{D}_{\mathrm{SBAS}}}$ and $\mathbf{C}_{\mathbf{V}_{\mathrm{SBAS}}}$, we need to determine $\mathbf{C}_{\boldsymbol{\phi}}$ first. In [19] and [26], an expression for each element of $\mathbf{C}_{\boldsymbol{\phi}}$ is given as

$$\mathbf{C}_{\boldsymbol{\phi}}\left(\phi_{i,j},\phi_{m,n}\right) = \mathrm{Cov}\left(\phi_{i,j},\phi_{m,n}\right) \approx \frac{1}{2L}\frac{\gamma_{i,m}\cdot\gamma_{j,n}-\gamma_{i,n}\cdot\gamma_{m,j}}{\gamma_{i,j}\cdot\gamma_{m,n}} \tag{28}$$

where $\phi_{i,j}$ and $\gamma_{i,j}$ are the interferometric phase and coherence between the ith and jth acquisitions, respectively, and $\phi_{m,n}$ and

Authorized licensed use limited to: Peking University. Downloaded on August 25,2026 at 14:45:26 UTC from IEEE Xplore. Restrictions apply.

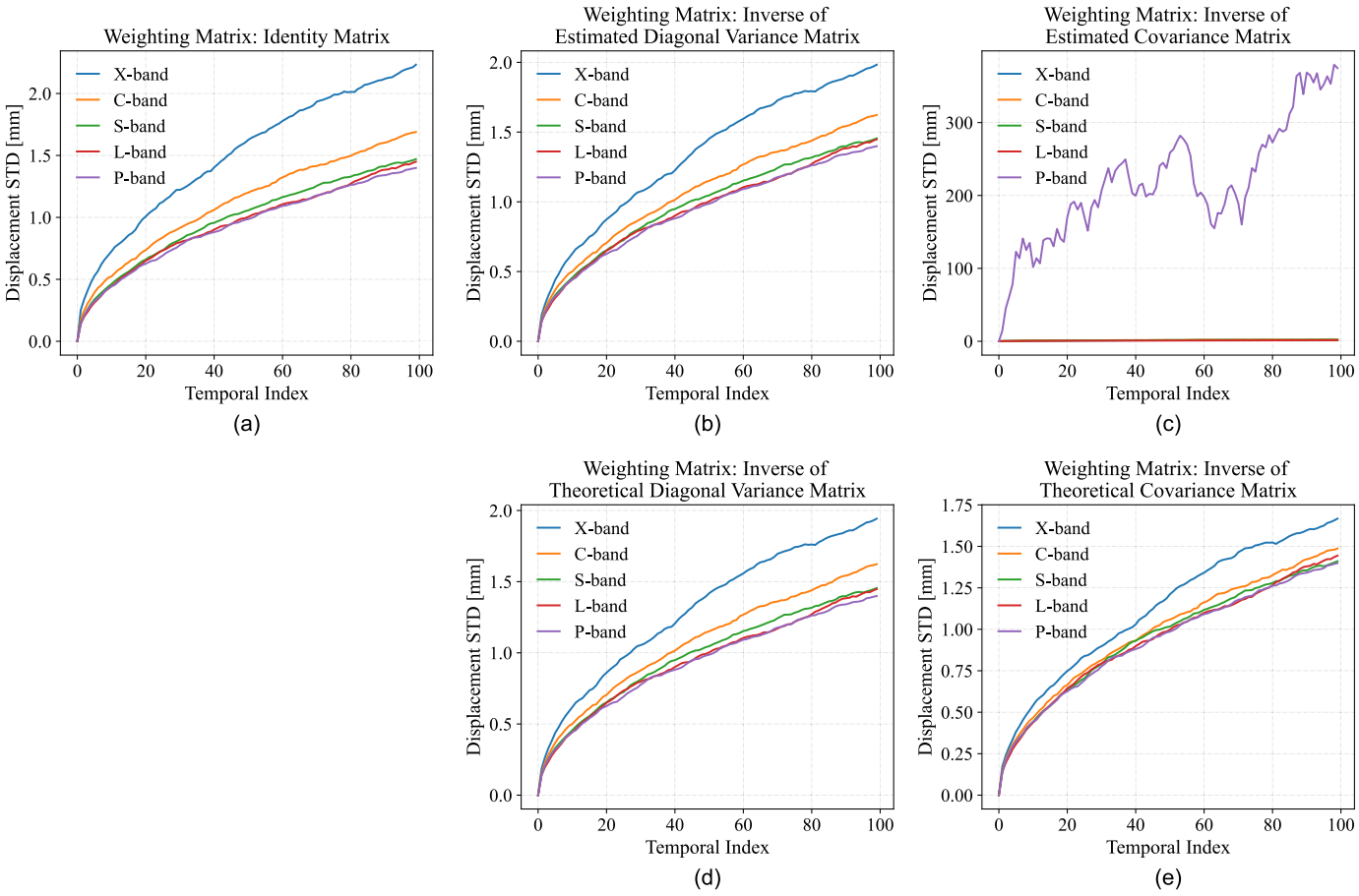

Fig. 6. Standard deviations of the displacement series obtained by SBAS for different wavelengths in simulation under two coherence schemes and three weighting schemes in (24). (a) Identity matrix, inverse matrix of the diagonal variance matrix calculated using (b) estimated coherence in simulation and (d) theoretical coherence, and inverse matrix of the covariance matrix calculated using (c) estimated coherence in simulation and (e) theoretical coherence. The network is formed by connecting six subsequent acquisitions but excludes pairs with a coherence below 0.25. The first acquisition is taken as the reference. Here, σ = 2.0 mm and the number of looks is 100.

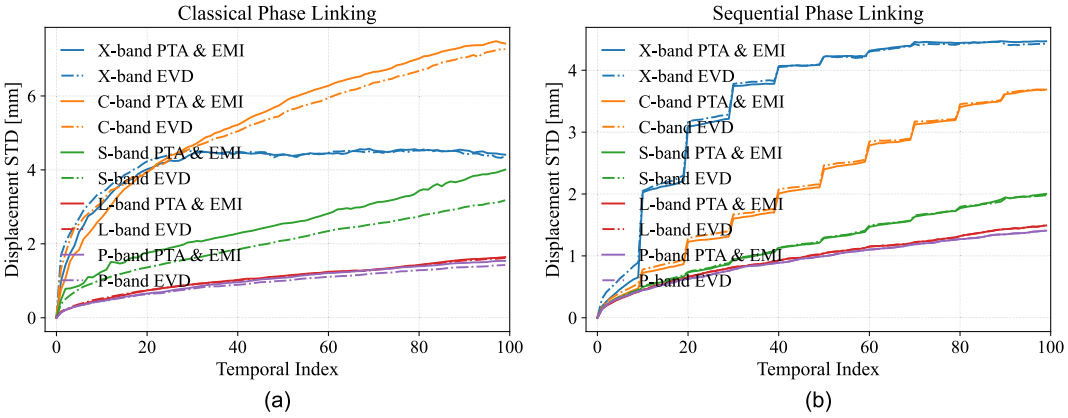

Fig. 7. Standard deviations of the displacement series obtained by (a) classical phase linking and (b) sequential phase linking for different wavelengths in simulation under three phase-linking methods: PTA, EVD, and EMI. Here, σ = 2.0 mm and the number of looks is 100.

$\gamma_{m,n}$ are those between the mth and nth acquisitions. When $i = m$ and $j = n$, $\mathrm{Cov}(\phi_{i,j}, \phi_{m,n})$ reduces to the variance of the interferometric phase or the diagonal element of $\mathbf{C}_{\boldsymbol{\phi}}$ [43]

$$\mathbf{C}_{\boldsymbol{\phi}}\left(\phi_{i,j}, \phi_{i,j}\right) = \mathrm{Var}\left(\phi_{i,j}, \phi_{i,j}\right) \approx \frac{1}{2L}\frac{1-\gamma_{i,j}^2}{\gamma_{i,j}^2}. \tag{29}$$

Equations (28) and (29) are commonly used to approximate the variance when L is large enough. Furthermore, for a given L, very low coherence can also lead to inaccurate estimations in (28) and (29). This issue can be mitigated by applying a coherence threshold filter. Substituting (11) and (13) into (28), the covariance becomes

$$\mathrm{Cov}\left(\varphi_{i,j}, \varphi_{m,n}\right) = \frac{1}{2L} \cdot \gamma\left(\lambda\right)^{|i-m|+|j-n|-|i-j|-|m-n|}$$

Authorized licensed use limited to: Peking University. Downloaded on August 25,2026 at 14:45:26 UTC from IEEE Xplore. Restrictions apply.

TABLE III

STANDARD DEVIATIONS OF THE VELOCITIES OBTAINED BY SBAS FOR DIFFERENT WAVELENGTHS IN SIMULATION UNDER DIFFERENT WEIGHTING SCHEMES. 1) IDENTITY MATRIX. 2) INVERSE MATRIX OF ESTIMATED DIAGONAL VARIANCE MATRIX. 3) INVERSE MATRIX OF ESTIMATED COVARIANCE MATRIX. 4) INVERSE MATRIX OF THEORETICAL DIAGONAL VARIANCE MATRIX. 5) INVERSE MATRIX OF THEORETICAL COVARIANCE MATRIX. THE NETWORK IS FULLY CONNECTED BUT EXCLUDES PAIRS WITH A COHERENCE BELOW 0.25. HERE, T_P = 12/365.25 YEAR AND UNIT OF STANDARD DEVIATION: MM/YR

	Weighting Matrix in (27)	Weighting Matrix in (24)					$\sqrt{\text{CRLB}}$
		1	2	3	4	5	
X-band (3.1 cm)	1	0.75	0.97	1.24	0.66	0.57	0.51
	2	0.80	0.97	1.26	0.70	0.60	
	3	0.65	0.80	1.00	0.57	0.49	
C-band (5.6 cm)	1	0.71	0.70	60.95	0.62	0.50	0.46
	2	0.74	0.71	71.34	0.65	0.53	
	3	0.62	0.59	5.70	0.53	0.43	
S-band (9.4 cm)	1	0.71	0.63	14.86	0.62	0.47	0.44
	2	0.76	0.66	18.52	0.64	0.51	
	3	0.62	0.54	4.17	0.53	0.41	
L-band (23.6 cm)	1	0.55	0.53	10.28	0.53	0.49	0.43
	2	0.57	0.53	8.91	0.53	0.50	
	3	0.47	0.44	1.69	0.44	0.41	
P-band (68.9 cm)	1	0.48	0.48	130.81	0.48	0.47	0.43
	2	0.50	0.50	152.72	0.50	0.49	
	3	0.42	0.41	16.96	0.41	0.41	

$$-\frac{1}{2L}\cdot\gamma(\lambda)^{|i-n|+|j-m|-|i-j|-|m-n|}. \quad (30)$$

Defining the index for the interferogram between the ith and jth acquisitions as $\text{Idx}(i,j)$, the covariance between the phase of the kth and lth acquisitions can be derived as

$$\text{Cov}(D_k, D_l) = \frac{\lambda^2}{16\pi^2}\sum_{i=1}^{N-1}\sum_{j=i+1}^{N}\sum_{m=1}^{N-1}\sum_{n=m+1}^{N} a_{k,ij}\cdot a_{l,mn} \cdot \text{Cov}\left(\phi_{i,j}, \phi_{m,n}\right) \quad (31)$$

where the coefficients $a_{k,ij}, a_{l,mn}$ are the elements of $(\mathbf{H}^{\mathrm{T}}\mathbf{W}\mathbf{H})^{-1}\mathbf{H}^{\mathrm{T}}\mathbf{W}$ at position $[k, \text{Idx}(i,j)]$ and $[l, \text{Idx}(m,n)]$. When $k = l$, (31) reduces to the variance of phase. The variance of velocity v can be derived as

$$\text{Var}(v) = \sum_{k=1}^{N}\sum_{l=1}^{N} b_{2,k}\cdot b_{2,l}\cdot \text{Cov}(D_k, D_l) \quad (32)$$

where $b_{2,k}$ and $b_{2,l}$ are the elements of $(\mathbf{H}_{\mathbf{D}}^{\mathrm{T}}\mathbf{W}_{\mathbf{D}}\mathbf{H}_{\mathbf{D}})^{-1}\mathbf{H}_{\mathbf{D}}^{\mathrm{T}}\mathbf{W}_{\mathbf{D}}$ at position $(2,k)$ and $(2,l)$.

The observation matrix $\mathbf{H}_{\boldsymbol{\phi}}$ depends on the network connecting the individual SAR acquisitions. A fully connected network would achieve the highest precision while maximizing the mitigation of bias introduced by the closure phase [20]. In practice, however, the number of connections is limited by issues such as decorrelation, phase-unwrapping errors, computational cost, and storage constraints. Here, we consider two scenarios:

1) a fully connected network, but excluding interferograms with a coherence smaller than 0.25, and
2) a network formed by connecting six subsequent acquisitions, also excluding interferograms with a coherence smaller than 0.25.

The weighting matrix $\mathbf{W}_{\boldsymbol{\phi}}$ can also be constructed in several ways. Ideally, it should be calculated as the inverse matrix of the covariance matrix $\mathbf{C}_{\boldsymbol{\phi}}$, which achieves the highest precision. In practice, however, it is limited by issues such as computational cost, the precision and accuracy of coherence estimation, and the numerical stability of computing the inverse of $\mathbf{C}_{\boldsymbol{\phi}}$. Here, we consider three different options for $\mathbf{W}_{\boldsymbol{\phi}}$:

1) the inverse matrix of $\mathbf{C}_{\boldsymbol{\phi}}$,
2) the inverse matrix of the diagonal variance matrix (by setting the nondiagonal elements of $\mathbf{C}_{\boldsymbol{\phi}}$ to zero), and
3) the identity matrix.

The variances of the displacement series for different wavelengths are compared in Figs. 2 and 3. For velocity, the corresponding results are listed in Tables I and II. In general, a longer wavelength achieves higher precision. Compared to options (2) and (3), using the inverse of the covariance matrix as the weighting matrix yields more precise results that are closer to the CRLB. This is attributed to the sensitivity of the WLS solution to the weighting matrix values. Without a precise weighting matrix, the estimation error cannot be effectively suppressed. Moreover, across different weighting

Authorized licensed use limited to: Peking University. Downloaded on August 25,2026 at 14:45:26 UTC from IEEE Xplore. Restrictions apply.

TABLE IV

STANDARD DEVIATIONS OF THE VELOCITIES OBTAINED BY SBAS FOR DIFFERENT WAVELENGTHS IN SIMULATION UNDER DIFFERENT WEIGHTING SCHEMES. 1) IDENTITY MATRIX. 2) INVERSE MATRIX OF ESTIMATED DIAGONAL VARIANCE MATRIX. 3) INVERSE MATRIX OF ESTIMATED COVARIANCE MATRIX. 4) INVERSE MATRIX OF THEORETICAL DIAGONAL VARIANCE MATRIX. 5) INVERSE MATRIX OF THEORETICAL COVARIANCE MATRIX. THE NETWORK IS FORMED BY CONNECTING SIX SUBSEQUENT ACQUISITIONS BUT EXCLUDES PAIRS WITH A COHERENCE BELOW 0.25. HERE, T_P = 12/365.25 YEAR AND UNIT OF STANDARD DEVIATION: MM/YR

	Weighting Matrix in (27)	Weighting Matrix in (24)					$\sqrt{\text{CRLB}}$
		1	2	3	4	5	
X-band (3.1 cm)	1	0.75	0.67	0.63	0.66	0.57	0.51
	2	0.80	0.71	0.68	0.70	0.60	
	3	0.65	0.58	0.55	0.57	0.49	
C-band (5.6 cm)	1	0.57	0.55	0.74	0.55	0.50	0.46
	2	0.59	0.57	0.86	0.57	0.53	
	3	0.49	0.47	0.52	0.47	0.43	
S-band (9.4 cm)	1	0.49	0.48	0.63	0.48	0.47	0.44
	2	0.53	0.52	0.70	0.52	0.51	
	3	0.43	0.43	0.48	0.43	0.41	
L-band (23.6 cm)	1	0.49	0.49	0.50	0.49	0.49	0.43
	2	0.50	0.50	0.51	0.50	0.50	
	3	0.42	0.42	0.42	0.42	0.41	
P-band (68.9 cm)	1	0.47	0.47	74.03	0.47	0.47	0.43
	2	0.49	0.49	120.11	0.49	0.49	
	3	0.41	0.41	0.92	0.41	0.41	

schemes, a longer wavelength exhibits greater stability and closer proximity to its corresponding CRLB. Even with a suboptimal weighting matrix, longer wavelengths still produce results close to the CRLB. Note that the relatively small displacement standard deviation observed here stems from the use of a large number of looks (100 looks). When the number of looks is reduced to 20 looks, the standard deviation of the last acquisition increases to approximately 5 mm.

Notably, the S-band results exhibit slightly higher errors than the C-band results in Fig. 2(a). Under the coherence threshold of 0.25, S-band uses 3059 interferograms compared to only 1209 for C-band, implying that more interferograms with higher phase errors are excluded in C-band. Without coherence filtering, S-band outperforms C-band. Coherence filtering provides more substantial optimization for shorter wavelengths, leading to the better performance of the C-band. A similar observation is found in the corresponding column of Table I.

E. Error Propagation of Phase Linking

The phase-linking technique generally refers to a class of algorithms used to optimize the phase series based on the Sample Covariance Matrix (SCM) $\mathbf{C}$ [33] whose elements can be defined by (2). The matrix $\mathbf{C}$ can thus be decomposed as the Hadamard product of the real coherence matrix $\mathbf{\Gamma}$ and the interferometric phase matrix $\boldsymbol{\phi}$. Algorithms such as Phase Triangulation Algorithm (PTA, also known as SqueeSAR) and Eigendecomposition-based Maximum-likelihood estimator of Interferometric phase (EMI) essentially formulate the problem as a Maximum-Likelihood-Estimation (MLE) problem [31], [33] while Eigen Value Decomposition approach (EVD, also known as CAESAR) is analogous to polarimetric decomposition in PolSAR and decomposes the covariance matrix through Principal Component Analysis (PCA) [32]. Although PTA and EMI stem from a similar framework, no closed-form solution exists for PTA, making it difficult to analytically derive the error of the resulting displacement series. For EVD, the eigendecomposition of $\mathbf{C}$ cannot yield a closed-form solution, leading to the same issue. Moreover, in the absence of coherence estimation error, PTA and EMI both achieve optimal performance, while EVD yields suboptimal results that deviate from the CRLB [33]. Consequently, EMI emerges as the most suitable benchmark for evaluating the performance of phase-linking methods. Therefore, our derivation is primarily based on the EMI algorithm.

The optimized phase for the ith acquisition obtained via EMI is given by

$$\hat{\varphi}_i = \angle \hat{\zeta}_i^{-1} \tag{33}$$

where $\boldsymbol{\zeta}$ is the eigenvector corresponding to the smallest eigenvalue of $|\mathbf{C}|^{-1} \circ \mathbf{C}$. To eigendecompose $|\mathbf{C}|^{-1} \circ \mathbf{C}$, we need to determine $\boldsymbol{\phi}$ first. The element of the interferometric phase

Authorized licensed use limited to: Peking University. Downloaded on August 25,2026 at 14:45:26 UTC from IEEE Xplore. Restrictions apply.

TABLE V

STANDARD DEVIATIONS OF THE VELOCITIES OBTAINED BY PHASE LINKING FOR DIFFERENT WAVELENGTHS IN SIMULATION UNDER DIFFERENT PHASE-LINKING ALGORITHMS AND DIFFERENT WEIGHTING SCHEMES IN (27). 1) IDENTITY MATRIX. 2) INVERSE MATRIX OF DIAGONAL VARIANCE MATRIX. 3) INVERSE MATRIX OF COVARIANCE MATRIX. HERE, T_P = 12/365.25 YEAR AND UNIT OF STANDARD DEVIATION: MM/YR

	Weighting Matrix in (27)	Phase Linking Algorithm				$\sqrt{\text{CRLB}}$
		PTA and EMI	EVD	Sequential PTA and EMI	Sequential EVD	
X-band (3.1 cm)	1	1.45	1.46	1.56	1.55	0.51
	2	0.89	0.86	1.14	1.13	
	3	0.80	0.86	1.09	1.09	
C-band (5.6 cm)	1	2.51	2.39	1.29	1.29	0.46
	2	2.41	2.30	1.18	1.20	
	3	1.95	2.72	1.10	1.22	
S-band (9.4 cm)	1	1.24	1.01	0.68	0.68	0.44
	2	1.38	1.12	0.67	0.67	
	3	1.14	1.00	0.73	0.71	
L-band (23.6 cm)	1	0.55	0.54	0.51	0.51	0.43
	2	0.56	0.56	0.52	0.52	
	3	0.47	0.47	0.44	0.44	
P-band (68.9 cm)	1	0.53	0.48	0.48	0.48	0.43
	2	0.54	0.50	0.50	0.50	
	3	0.45	0.42	0.42	0.42	

matrix at position (m, n) is given by

$$\phi_{m,n} = \exp\left\{\mathrm{j}\cdot\left[-\frac{4\pi}{\lambda}D(m,n)+\delta_\phi(m,n)\right]\right\} \tag{34}$$

where $D(m, n)$ is the displacement, and $\delta_\phi(m, n)$ is the phase noise. As in (20), the displacement is assumed to increase linearly with time at a constant velocity v. Then (34) becomes

$$\phi_{m,n} = \exp\left\{\mathrm{j}\cdot\left[\frac{4\pi v}{\lambda}(n-m)\,t_p+\delta_\phi(m,n)\right]\right\}. \tag{35}$$

Now the matrix $|\mathbf{C}|^{-1}\circ\mathbf{C}$ can be decomposed as

$$|\mathbf{C}|^{-1}\circ\mathbf{C} = \mathbf{\Gamma}^{-1}\circ\mathbf{\Gamma}\circ\boldsymbol{\phi} = \mathbf{V}^{-1}\mathbf{M}\mathbf{V}. \tag{36}$$

Here, we take the first acquisition as the reference; then, $\mathbf{V}$ is given by

$$\mathbf{V} = \mathrm{diag}\left\{1, e^{\mathrm{j}\cdot\left[\frac{4\pi v t_p}{\lambda}-\sum_{k=2}^{2}\delta_\phi(k-1,k)\right]},\ldots,\right.$$
$$\left. e^{\mathrm{j}\cdot\left[\frac{4(N-1)\pi v t_p}{\lambda}-\sum_{k=2}^{N}\delta_\phi(k-1,k)\right]}\right\} \tag{37}$$

and $\mathbf{M}$ is a real coefficient matrix given by

$$\mathbf{M} = \frac{1}{1-\gamma(\lambda)^2}\times\begin{bmatrix} 1 & -\gamma(\lambda)^2 & \cdots & 0 & 0 \\ -\gamma(\lambda)^2 & 1+\gamma(\lambda)^2 & \cdots & 0 & 0 \\ \vdots & \vdots & \ddots & \vdots & \vdots \\ 0 & 0 & \cdots & 1+\gamma(\lambda)^2 & -\gamma(\lambda)^2 \\ 0 & 0 & \cdots & -\gamma(\lambda)^2 & 1 \end{bmatrix}. \tag{38}$$

Therefore, the complex phase component resulting from the eigenvalue decomposition depends solely on $\mathbf{V}$. The phase series optimized by EMI is

$$\boldsymbol{\varphi}_{\mathrm{EMI}} = \left[0, -\frac{4\pi v t_p}{\lambda}+\sum_{k=2}^{2}\delta_\phi(k-1,k),\cdots,\right.$$
$$\left.-\frac{4(N-1)\pi v t_p}{\lambda}+\sum_{k=2}^{N}\delta_\phi(k-1,k)\right]^{\mathrm{T}}. \tag{39}$$

According to (28), the covariance matrix of $\boldsymbol{\varphi}_{\mathrm{EMI}}$ can be derived as

$$\mathbf{C}_{\boldsymbol{\varphi}_{\mathrm{EMI}}} = \frac{1-\gamma(\lambda)^2}{2L\gamma(\lambda)^2}\begin{bmatrix} 0 & 0 & \cdots & 0 & 0 \\ 0 & 1 & \cdots & 1 & 1 \\ \vdots & \vdots & \ddots & \vdots & \vdots \\ 0 & 1 & \cdots & N-2 & N-2 \\ 0 & 1 & \cdots & N-2 & N-1 \end{bmatrix}. \tag{40}$$

Authorized licensed use limited to: Peking University. Downloaded on August 25,2026 at 14:45:26 UTC from IEEE Xplore. Restrictions apply.

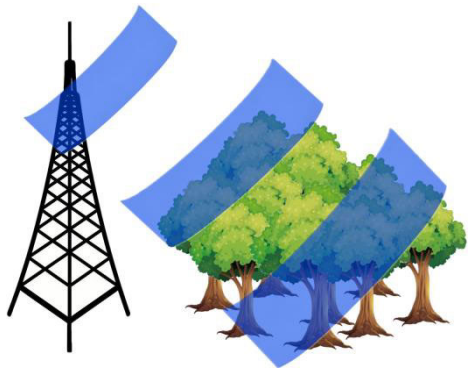

Fig. 8. Observation geometry of TropiSCAT and the three distinct regions. (Left) tower, (middle) foliage only, and (right) full forest. Modified from [45].

Substituting (13) into (40), the covariance matrix of the displacement series obtained via EMI is given by

$$\mathbf{C}_{\mathbf{D}_{\text{EMI}}} = k(\lambda)\begin{bmatrix} 0 & 0 & \cdots & 0 & 0 \\ 0 & 1 & \cdots & 1 & 1 \\ \vdots & \vdots & \ddots & \vdots & \vdots \\ 0 & 1 & \cdots & N-2 & N-2 \\ 0 & 1 & \cdots & N-2 & N-1 \end{bmatrix}. \tag{41}$$

A key observation is that, by taking the first acquisition as the reference in (18), (41) is actually equivalent to (18), i.e.,

$$\begin{aligned} \text{CRLB}_{\mathbf{D}}(\lambda) &= k(\lambda)\cdot\left(\boldsymbol{\Theta}^{\text{T}}\mathbf{Y}(1{:}N, 1{:}N)\,\boldsymbol{\Theta}\right)^{-1} \\ &= \mathbf{C}_{\mathbf{D}_{\text{EMI}}}(1{:}N, 1{:}N) \end{aligned} \tag{42}$$

where $\mathbf{Y}(1{:}N, 1{:}N)$ and $\mathbf{C}_{\mathbf{D}_{\text{EMI}}}(1{:}N, 1{:}N)$ denote the submatrix of $\mathbf{Y}$ and $\mathbf{C}_{\mathbf{D}_{\text{EMI}}}$ obtained by removing their first row and first column, respectively. This is because (36) employs the exact coherence matrix $\boldsymbol{\Gamma}$, in which case the EMI result attains the CRLB, as reflected in the simulation results in [33]. As in SBAS, the covariance matrix for the initial displacement D_1 and constant velocity v can be derived as

$$\mathbf{C}_{\mathbf{V}_{\text{EMI}}} = \left(\mathbf{H}_{\mathbf{D}}^{\text{T}}\mathbf{W}_{\mathbf{D}}\mathbf{H}_{\mathbf{D}}\right)^{-1}\mathbf{H}_{\mathbf{D}}^{\text{T}}\mathbf{W}_{\mathbf{D}}\mathbf{C}_{\mathbf{D}_{\text{EMI}}}\mathbf{W}_{\mathbf{D}}\mathbf{H}_{\mathbf{D}}\left(\mathbf{H}_{\mathbf{D}}^{\text{T}}\mathbf{W}_{\mathbf{D}}\mathbf{H}_{\mathbf{D}}\right)^{-1}. \tag{43}$$

Similarly, by taking the inverse of the covariance matrix as the weighting matrix in (43) and taking the first acquisition as the reference in (22), (43) is equivalent to (22).

According to the results in Section II-C, both the variances of displacement and velocity obtained by EMI decrease as the wavelength increases, implying the superiority of long wavelengths. An example is shown in Fig. 1(b).

III. Simulations

In this section, we conduct simulation experiments to validate the findings of Section II. The basic configurations of the simulations are as follows.

1) There are L SHPs. Each pixel represents a resolution cell and contains M independent, uniformly distributed elementary scatterers as defined in (1), following the first-order Born approximation.
2) The reflectivity of each elementary scatterer is assumed to follow the same zero-mean complex circular Gaussian distribution.
3) Each elementary scatterer's signal also includes a phase component corresponding to its initial range distance to the antenna phase center and its random motion. The only change in the scatterer between different acquisitions is its random motion. For the kth acquisition, the random motion in the LOS direction follows a Gaussian distribution of $N(0, (k-1)\sigma^2)$.

In the simulations, we established systems spanning X- to P-band. The wavelengths and observation geometry were configured to match those of mainstream satellite SAR systems. The revisit period was set to 12 days, identical to that of Sentinel-1. These configurations ensure that the simulation is comparable to real observation scenarios.

We run SBAS and phase-linking algorithms on the simulated data to retrieve the displacement series and velocity. For SBAS, we constructed two connected networks under three weighting schemes as in Section II-D. Here, we also employed coherence obtained through different approaches to compute the corresponding weighting matrices:

1) Estimated coherence using simulated time-series data, and
2) theoretical coherence computed using (10).

For phase linking, we employed the PTA, EVD, and EMI algorithms, along with their corresponding sequential estimators [33], [34], to obtain the optimized phase series.

We set $L = 100$, $M = 1000$, and $\sigma = 2.0$ mm. We simulated $N = 100$ acquisitions in total, and assumed that the true displacement is zero for simplicity. For each wavelength, we performed 1000 Monte Carlo simulations to compute the Root Mean Square Error (RMSE) as a measure of the standard deviation of the estimated results.

The average coherence and phase standard deviation of the interferograms between the first and subsequent acquisitions are computed and shown in Fig. 4. As expected, the estimated coherence is biased toward higher values, particularly when the coherence is low [44]. The phase standard deviations agree well with their theoretical values, as shown in Fig. 4(b).

The standard deviations of the displacement series solved by SBAS are shown in Figs. 5 and 6. In general, a longer wavelength yields a lower displacement error. As mentioned in Section II-D, coherence filtering provides more substantial optimization for shorter wavelengths, resulting in reduced performance differences between S- and C-bands as shown in Fig. 5(a) and (d). In Fig. 5(b) and (c), the estimated coherence, which is subject to random errors and bias, is used to compute the weighting matrix. It leads to a higher standard deviation in the displacement series. This problem can be significant due to numerical instabilities, as shown in Fig. 5(c). Instead, Fig. 5(d) and (e) do not have such problems, as theoretical coherence is used. Similar observations can be found in Fig. 6.

The standard deviations of the displacement series estimated by phase linking are shown in Fig. 7. A longer wavelength again generally leads to a smaller error. However, the final estimation precision is also affected by numerical instabilities arising from the estimation of the SCM $\mathbf{C}$. According to the principles of different phase-linking algorithms, PTA and EMI rely on matrix $|\mathbf{C}|^{-1}\circ\mathbf{C}$, whereas EVD uses only $\mathbf{C}$. Since $|\mathbf{C}|^{-1}\circ\mathbf{C}$ exhibits greater numerical instability than $\mathbf{C}$, PTA and

Authorized licensed use limited to: Peking University. Downloaded on August 25,2026 at 14:45:26 UTC from IEEE Xplore. Restrictions apply.

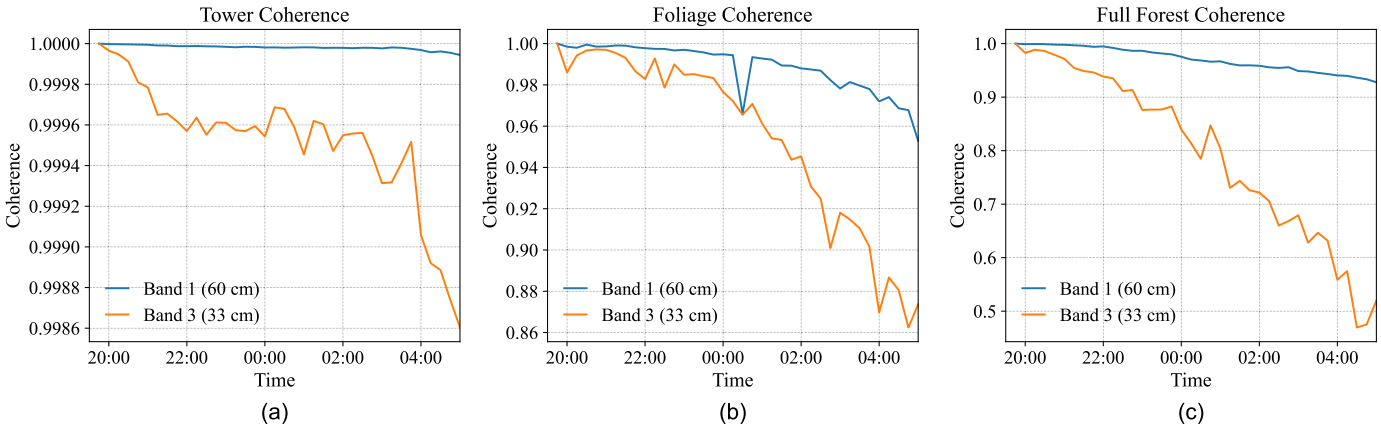

Fig. 9. Coherence of TropiSCATAQ7 HV polarization data in different regions. (a) Tower, (b) foliage, and (c) full forest, computed for the time interval October 10–11, 2011.

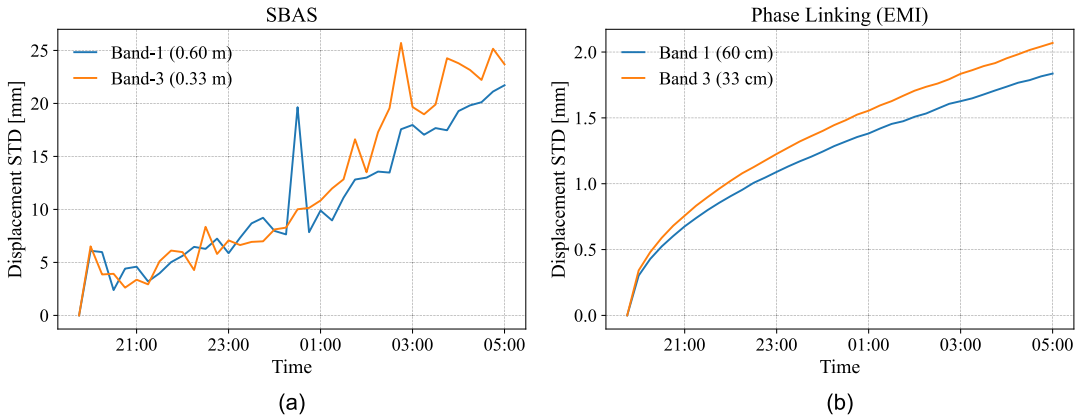

Fig. 10. Standard deviation of displacement series estimated by SBAS and phase linking using TropiSCAT data. (a) SBAS. (b) EMI. The result in (b) was computed using the random motion between consecutive observations (σ_p) estimated in Table VI. The number of looks in SBAS and EMI is 1 and 27, respectively. The same dataset as in Fig. 9 was used here.

EMI consequently exhibit slightly lower precision compared to EVD, as shown in Fig. 7(a). In contrast, sequential phase linking mitigates the impact of numerical instability in the full SCM by partitioning the original time-series data into ministacks, resulting in overall higher precision compared to classical methods. Furthermore, in Fig. 7(a), the X-band results approach a constant standard deviation because, starting from acquisition 20, the subsequent acquisitions nearly completely decorrelate with the first acquisition, thereby rendering the associated standard deviations meaningless. Sequential phase linking is free of this problem, as shown in Fig. 7(b).

Consistent with the displacement series, the results in Tables III–V show that the velocity precision generally improves with a longer wavelength for both SBAS and phase linking. A properly selected, higher precision weighting matrix can yield higher estimation precision. The limited number of Monte Carlo trials (1000 repetitions) introduces errors in the computed standard deviations, which can sometimes be even smaller than the square root of the CRLB.

IV. Observations in Real-Data Experiments

To validate the theories in Section II, the following requirements should be fulfilled:

1) The radars working across different wavelengths should "see" the same scatterers on the ground, and
2) the data at different wavelengths should be acquired simultaneously.

These requirements render validation using real-world SAR data almost impossible.

Alternatively, multiband tower-based scatterometers provide excellent opportunities for validating the theories. A fundamental distinction between SAR and scatterometers lies in their data acquisition techniques and resulting resolutions: SAR employs the synthetic aperture technique to achieve high azimuth resolution, whereas a scatterometer typically does not use aperture synthesis. However, these differences do not affect the scattering mechanism information embedded in the data, which is our primary interest. Here, we use multiband data acquired by the TropiSCAT experiment [45]. TropiSCAT is a scatterometer experiment deployed in a tropical rainforest in French Guiana to support the definition of the BIOMASS mission for global forest biomass estimation [45]. A primary objective of TropiSCAT is measuring temporal coherence in the HH, VV, and HV polarizations at intervals on the order of 15 min (t_p = 15 min), spanning daily and monthly scales. The observation geometry of TropiSCAT is shown in Fig. 8.

The TropiSCAT system acquires backscattering data across a continuous frequency spectrum from 400 to 1000 MHz. The data are released in three bands, each with a bandwidth of 200 MHz, designated as follows:

Authorized licensed use limited to: Peking University. Downloaded on August 25,2026 at 14:45:26 UTC from IEEE Xplore. Restrictions apply.

TABLE VI
STANDARD DEVIATION OF SCATTERERS' RANDOM MOTION. 1) RANDOM MOTION BETWEEN CONSECUTIVE OBSERVATIONS (σ_p). 2) TOTAL RANDOM MOTION (σ)

	Standard Deviation [mm]	Tower	Foliage Only	Full Forest
Band 1 (P-band)	1	~ 0	1.78	2.81
	2	~ 0	10.80	17.11
Band 3 (L-band)	1	~ 0	2.03	4.57
	2	~ 0	12.34	27.83

1) Band 1, with a center frequency of 500 MHz, or a wavelength of approximately 0.6 m,
2) band 2, with a center frequency of 700 MHz, or a wavelength of approximately 0.43 m, and
3) band 3, with a center frequency of 900 MHz, or a wavelength of approximately 0.33 m.

We use Band 1 and Band 3, as their wavelengths closely approximate those of the P-band and L-band satellite SAR missions.

The TropiSCAT system can acquire data in four polarizations, but we only use VH polarization since it is sensitive to vegetation structure and less affected by double-bounce scattering. The dielectric constant of the forest changes dynamically during a day primarily due to the varying tree water content as a result of forest physiology. However, the physiological activity of the trees is quiescent at nighttime, as found in [46] and [47]. Therefore, we only use nighttime data acquired from 19:45 P.M. to 05:00 A.M. (38 acquisitions). Furthermore, by referring to meteorological records, we select only the data acquired during periods of stable weather conditions characterized by the absence of precipitation and low wind-speed variability.

The raw TropiSCAT frequency-domain echoes are transformed into the range domain via a Fourier transform to extract the slant-range backscattering profile. The range pixel size is 0.75 m. Following established practice [45], we divide the data into the following three distinct regions in the range direction as shown in Fig. 8:

1) The tower region, 0–15 m, 20 pixels,
2) the foliage-only region, 30–50 m, 27 pixels, and
3) the full-forest region, 60–80 m, 27 pixels.

Our primary region of interest is the foliage-only region.

A. Analysis of Decorrelation Mechanism

Here, we analyze the possible decorrelation sources in (3). The TropiSCAT system on top of a tower maintains an invariant spatial position and observation geometry across all acquisitions in stable weather conditions. Consequently, there is no geometry and volume decorrelation. The system has an extremely low thermal noise level of approximately −105 dBm, significantly lower than the backscattering intensity from the forest scene [45], rendering the contribution of thermal decorrelation negligible. There is also no decorrelation associated with SAR and InSAR processing steps, except for quantization.

Fig. 9 shows the computed coherence for Band 1 and Band 3 across the tower, foliage only, and full-forest regions. The tower region can be assumed to be stationary and to have a constant dielectric constant, leading to negligible temporal decorrelation. Its high coherence demonstrates that the contributions from thermal noise decorrelation, quantization decorrelation, and ambiguity decorrelation are negligible. The conclusion associated with ambiguity decorrelation also applies to the foliage-only region. The thermal noise decorrelation and quantization decorrelation should also be very small for the foliage-only region, considering its strong reflectivity. To summarize, all contributions from nontemporal decorrelation sources are negligible.

For the temporal decorrelation in the foliage-only region, we do not expect the addition or removal of scatterers over the course of a night. The change in the dielectric constant is also insignificant at night, as explained previously. Therefore, the dominant temporal decorrelation mechanism should be random motion in the foliage-only region at nighttime. To further verify this assumption, we compute the equivalent standard deviation of the random motion for the data shown in Fig. 9 using (10) via logarithmic fitting. The results are presented in Table VI. For the foliage-only region, where the observed scatterers consist of fine, relatively uniform twigs and leaves across both bands, the retrieved standard deviations for Band 1 and Band 3 are very close. In addition, both the σ_p and the total σ are within reasonable ranges. In contrast, the backscattered signal from the full-forest region comprises contributions from a heterogeneous mixture of leaves, branches, trunks, and ground scatterers. In addition, the contribution from each type of scatterer to the total backscattered signal varies with wavelength. Consequently, the equivalent standard deviations differ significantly for Band 1 and Band 3 in this region.

B. Error of Displacement Series

Here, we use the same dataset as in Section IV-A to perform time-series analysis. For SBAS processing, we constructed a fully connected network. We estimated the displacement series using a weighting matrix calculated as the inverse matrix of the diagonal variance matrix. We set the number of looks to one because we only have 27 pixels per acquisition, but need to compute the standard deviation using the estimated displacement series. Therefore, we ran SBAS 27 times and

Authorized licensed use limited to: Peking University. Downloaded on August 25,2026 at 14:45:26 UTC from IEEE Xplore. Restrictions apply.

obtained 27 groups of displacement series, which were then used to compute the standard deviation of each epoch. The results in Fig. 10(a) shows the lower noise level of long-wavelength results.

For phase linking, we used the EMI algorithm to estimate the displacement series. However, we do not have enough data to compute a standard deviation for each acquisition in the displacement series. Therefore, we used the following approach to estimate a standard deviation instead. All available data were processed in a single run of EMI. Since no displacements actually occurred, we computed a single standard deviation using the estimated displacements for all epochs. The standard deviations of Band 1 and Band 3 are 2.92 and 3.40 mm, respectively, again showing the lower noise level of long-wavelength results.

In addition, using the random motion between consecutive observations (σ_p) estimated earlier, a theoretical error was computed for the displacement series. The result is shown in Fig. 10(b). This result also demonstrates the better performance of a longer wavelength.

To summarize, these results collectively confirm that, under identical conditions of random motion, the longer wavelength system can achieve a higher precision in measuring displacement with time-series techniques.

V. Conclusion

The relationship between the precision of InSAR time series and radar wavelength is a fundamental question, particularly in the multiband satellite SAR era. Assuming a distributed target, this work focuses on the effect of temporal decorrelation due to random motion of scatterers within a SAR resolution cell on the precision of the displacement series and velocity. Theoretical analysis shows that the CRLB for the displacement series and velocity decreases with increasing wavelength, implying that higher precision can be achieved using a SAR system with a longer wavelength. Consistent with the CRLB, time-series analysis methods, including SBAS and phase linking, also yield higher precision results with data from a longer wavelength system. Results from simulation and real-data experiments also support this conclusion. In terms of the effects of random-motion-induced temporal decorrelation, the findings of this work provide theoretical support for the flourishing of L-band satellite SAR systems, as well as implications for developing methods to fuse InSAR results from multiband systems.

Acknowledgment

The authors thank the European Space Agency (ESA) and the Center National d'Études Spatiales (CNES) for providing open access to the TropiSCAT data. They also thank Dr. Yang Lei from the National Space Science Center, Chinese Academy of Sciences, for helpful discussions on the decorrelation mechanisms of vegetation.

References

[1] T. Tadono, M. Ohki, T. Motohka, A. Rosenqvist, and S. Sobue, "Advanced Land Observing Satellite-2 'DAICHI-,' (ALOS-2): Overview and operational status," *IEEE Geosci. Remote Sens. Mag.*, vol. 13, no. 2, pp. 41–48, Jun. 2025, doi: 10.1109/MGRS.2025.3535720.

[2] R. Wang et al., "LuTan-1: An innovative L-band spaceborne bistatic interferometric synthetic aperture radar mission," *IEEE Geosci. Remote Sens. Mag.*, vol. 13, no. 2, pp. 58–78, Jun. 2025, doi: 10.1109/MGRS.2024.3478761.

[3] M. Ohki, T. Motohka, Y. Kankaku, S. H. Miura, T. Tadono, and Y. Arikawa, "Advanced Land Observing Satellite-4: Mission concepts and technical overview: Pioneering a new era of L-band SAR," *IEEE Geosci. Remote Sens. Mag.*, vol. 13, no. 2, pp. 35–40, Jun. 2025, doi: 10.1109/MGRS.2025.3529037.

[4] P. A. Rosen et al., "The NASA-ISRO SAR mission: A summary," *IEEE Geosci. Remote Sens. Mag.*, vol. 13, no. 2, pp. 8–34, Jun. 2025, doi: 10.1109/MGRS.2025.3578258.

[5] S. Quegan et al., "The European space agency BIOMASS mission: Measuring forest above-ground biomass from space," *Remote Sens. Environ.*, vol. 227, pp. 44–60, Jun. 2019, doi: 10.1016/j.rse.2019.03.032.

[6] E. Rodriguez and J. M. Martin, "Theory and design of interferometric synthetic aperture radars," *IEE Proc. F (Radar Signal Process.)*, vol. 139, no. 2, pp. 147–159, Apr. 1992, doi: 10.1049/ip-f-2.1992.0018.

[7] D. Massonnet and K. L. Feigl, "Discrimination of geophysical phenomena in satellite radar interferograms," *Geophys. Res. Lett.*, vol. 22, no. 12, pp. 1537–1540, Jun. 1995, doi: 10.1029/95GL00711.

[8] R. M. Goldstein, "Atmospheric limitations to repeat-track radar interferometry," *Geophys. Res. Lett.*, vol. 22, no. 18, pp. 2517–2520, Sep. 1995, doi: 10.1029/95GL02475.

[9] H. Tarayre and D. Massonnet, "Atmospheric propagation heterogeneities revealed by ERS-1 interferometry," *Geophys. Res. Lett.*, vol. 23, no. 9, pp. 989–992, May 1996, doi: 10.1029/96gl00622.

[10] P. A. Rosen, S. Hensley, H. A. Zebker, F. H. Webb, and E. J. Fielding, "Surface deformation and coherence measurements of Kilauea Volcano, Hawaii, from SIR-C radar interferometry," *J. Geophys. Res.*, vol. 101, no. E10, pp. 23109–23125, 1996, doi: 10.1029/96JE01459.

[11] H. A. Zebker, P. A. Rosen, and S. Hensley, "Atmospheric effects in interferometric synthetic aperture radar surface deformation and topographic maps," *J. Geophys. Res., Solid Earth*, vol. 102, no. B4, pp. 7547–7563, Apr. 1997, doi: 10.1029/96jb03804.

[12] C. J. DiCaprio and M. Simons, "Importance of ocean tidal load corrections for differential InSAR," *Geophys. Res. Lett.*, vol. 35, no. 22, Nov. 2008, Art. no. L22309, doi: 10.1029/2008gl035806.

[13] X. Xu and D. T. Sandwell, "Toward absolute phase change recovery with InSAR: Correcting for Earth tides and phase unwrapping ambiguities," *IEEE Trans. Geosci. Remote Sens.*, vol. 58, no. 1, pp. 726–733, Jan. 2020, doi: 10.1109/TGRS.2019.2940207.

[14] O. L. Stephenson, Y.-K. Liu, Z. Yunjun, M. Simons, P. Rosen, and X. Xu, "The impact of plate motions on long-wavelength InSAR-derived velocity fields," *Geophys. Res. Lett.*, vol. 49, no. 21, Nov. 2022, Art. no. e2022GL099835, doi: 10.1029/2022gl099835.

[15] S. Zwieback, S. Hensley, and I. Hajnsek, "Assessment of soil moisture effects on L-band radar interferometry," *Remote Sens. Environ.*, vol. 164, pp. 77–89, Jul. 2015, doi: 10.1016/j.rse.2015.04.012.

[16] S. Zwieback and I. Hajnsek, "Influence of vegetation growth on the polarimetric zero-baseline DInSAR phase diversity—Implications for deformation studies," *IEEE Trans. Geosci. Remote Sens.*, vol. 54, no. 5, pp. 3070–3082, May 2016, doi: 10.1109/TGRS.2015.2511118.

[17] G. Gomba, A. Parizzi, F. De Zan, M. Eineder, and R. Bamler, "Toward operational compensation of ionospheric effects in SAR interferograms: The split-spectrum method," *IEEE Trans. Geosci. Remote Sens.*, vol. 54, no. 3, pp. 1446–1461, Mar. 2016, doi: 10.1109/TGRS.2015.2481079.

[18] C. Liang, P. Agram, M. Simons, and E. J. Fielding, "Ionospheric correction of InSAR time series analysis of C-band Sentinel-1 TOPS data," *IEEE Trans. Geosci. Remote Sens.*, vol. 57, no. 9, pp. 6755–6773, Sep. 2019, doi: 10.1109/TGRS.2019.2908494.

[19] F. De Zan, M. Zonno, and P. López-Dekker, "Phase inconsistencies and multiple scattering in SAR interferometry," *IEEE Trans. Geosci. Remote Sens.*, vol. 53, no. 12, pp. 6608–6616, Dec. 2015, doi: 10.1109/TGRS.2015.2444431.

[20] H. Ansari, F. De Zan, and A. Parizzi, "Study of systematic bias in measuring surface deformation with SAR interferometry," *IEEE Trans. Geosci. Remote Sens.*, vol. 59, no. 2, pp. 1285–1301, Feb. 2021, doi: 10.1109/TGRS.2020.3003421.

[21] H. A. Zebker and J. Villasenor, "Decorrelation in interferometric radar echoes," *IEEE Trans. Geosci. Remote Sens.*, vol. 30, no. 5, pp. 950–959, Sep. 1992, doi: 10.1109/36.175330.

[22] R. Bamler and M. Eineder, "Accuracy of differential shift estimation by correlation and split-bandwidth interferometry for wideband and delta-k SAR systems," *IEEE Geosci. Remote Sens. Lett.*, vol. 2, no. 2, pp. 151–155, Apr. 2005, doi: 10.1109/LGRS.2004.843203.

Authorized licensed use limited to: Peking University. Downloaded on August 25,2026 at 14:45:26 UTC from IEEE Xplore. Restrictions apply.

[23] A. Ferretti, C. Prati, and F. Rocca, "Permanent scatterers in SAR interferometry," *IEEE Trans. Geosci. Remote Sens.*, vol. 39, no. 1, pp. 8–20, Jan. 2001, doi: 10.1109/36.898661.
[24] M. Wei and D. T. Sandwell, "Decorrelation of L-band and C-band interferometry over vegetated areas in California," *IEEE Trans. Geosci. Remote Sens.*, vol. 48, no. 7, pp. 2942–2952, Jul. 2010, doi: 10.1109/TGRS.2010.2043442.
[25] M. Lavalle, M. Simard, and S. Hensley, "A temporal decorrelation model for polarimetric radar interferometers," *IEEE Trans. Geosci. Remote Sens.*, vol. 50, no. 7, pp. 2880–2888, Jul. 2012, doi: 10.1109/TGRS.2011.2174367.
[26] F. Rocca, "Modeling interferogram stacks," *IEEE Trans. Geosci. Remote Sens.*, vol. 45, no. 10, pp. 3289–3299, Oct. 2007, doi: 10.1109/TGRS.2007.902286.
[27] M. Neumann, L. Ferro-Famil, and A. Reigber, "Estimation of forest structure, ground, and canopy layer characteristics from multibaseline polarimetric interferometric SAR data," *IEEE Trans. Geosci. Remote Sens.*, vol. 48, no. 3, pp. 1086–1104, Mar. 2010, doi: 10.1109/TGRS.2009.2031101.
[28] Y. Morishita and R. F. Hanssen, "Temporal decorrelation in L-, C-, and X-band satellite radar interferometry for pasture on drained peat soils," *IEEE Trans. Geosci. Remote Sens.*, vol. 53, no. 2, pp. 1096–1104, Feb. 2015, doi: 10.1109/TGRS.2014.2333814.
[29] P. Berardino, G. Fornaro, R. Lanari, and E. Sansosti, "A new algorithm for surface deformation monitoring based on small baseline differential SAR interferograms," *IEEE Trans. Geosci. Remote Sens.*, vol. 40, no. 11, pp. 2375–2383, Nov. 2002, doi: 10.1109/TGRS.2002.803792.
[30] A. Monti Guarnieri and S. Tebaldini, "On the exploitation of target statistics for SAR interferometry applications," *IEEE Trans. Geosci. Remote Sens.*, vol. 46, no. 11, pp. 3436–3443, Nov. 2008, doi: 10.1109/TGRS.2008.2001756.
[31] A. Ferretti, A. Fumagalli, F. Novali, C. Prati, F. Rocca, and A. Rucci, "A new algorithm for processing interferometric data-stacks: SqueeSAR," *IEEE Trans. Geosci. Remote Sens.*, vol. 49, no. 9, pp. 3460–3470, Sep. 2011, doi: 10.1109/TGRS.2011.2124465.
[32] G. Fornaro, S. Verde, D. Reale, and A. Pauciullo, "CAESAR: An approach based on covariance matrix decomposition to improve multibaseline–multitemporal interferometric SAR processing," *IEEE Trans. Geosci. Remote Sens.*, vol. 53, no. 4, pp. 2050–2065, Apr. 2015, doi: 10.1109/TGRS.2014.2352853.
[33] H. Ansari, F. De Zan, and R. Bamler, "Efficient phase estimation for interferogram stacks," *IEEE Trans. Geosci. Remote Sens.*, vol. 56, no. 7, pp. 4109–4125, Jul. 2018, doi: 10.1109/TGRS.2018.2826045.
[34] H. Ansari, F. De Zan, and R. Bamler, "Sequential estimator: Toward efficient InSAR time series analysis," *IEEE Trans. Geosci. Remote Sens.*, vol. 55, no. 10, pp. 5637–5652, Oct. 2017, doi: 10.1109/TGRS.2017.2711037.
[35] Z. Yunjun, H. Fattahi, and F. Amelung, "Small baseline InSAR time series analysis: Unwrapping error correction and noise reduction," *Comput. Geosci.*, vol. 133, Dec. 2019, Art. no. 104331, doi: 10.1016/j.cageo.2019.104331.
[36] S. Mirzaee, F. Amelung, and H. Fattahi, "Non-linear phase linking using joined distributed and persistent scatterers," *Comput. Geosci.*, vol. 171, Feb. 2023, Art. no. 105291, doi: 10.1016/j.cageo.2022.105291.
[37] G. Krieger et al., "TanDEM-X: A satellite formation for high-resolution SAR interferometry," *IEEE Trans. Geosci. Remote Sens.*, vol. 45, no. 11, pp. 3317–3341, Nov. 2007, doi: 10.1109/TGRS.2007.900693.
[38] D. Just and R. Bamler, "Phase statistics of interferograms with applications to synthetic aperture radar," *Appl. Opt.*, vol. 33, no. 20, pp. 4361–4368, Jul. 1994, doi: 10.1364/ao.33.004361.
[39] P. Rizzoli, L. Dell'Amore, J.-L. Bueso-Bello, N. Gollin, D. Carcereri, and M. Martone, "On the derivation of volume decorrelation from TanDEM-X bistatic coherence," *IEEE J. Sel. Topics Appl. Earth Observ. Remote Sens.*, vol. 15, pp. 3504–3518, 2022, doi: 10.1109/JSTARS.2022.3170076.
[40] F. Gatelli, A. Monti Guarnieri, F. Parizzi, P. Pasquali, C. Prati, and F. Rocca, "The wavenumber shift in SAR interferometry," *IEEE Trans. Geosci. Remote Sens.*, vol. 32, no. 4, pp. 855–865, Jul. 1994, doi: 10.1109/36.298013.
[41] A. Monti Guarnieri and S. Tebaldini, "Hybrid Cramér–Rao bounds for crustal displacement field estimators in SAR interferometry," *IEEE Signal Process. Lett.*, vol. 14, no. 12, pp. 1012–1015, Dec. 2007, doi: 10.1109/LSP.2007.904705.
[42] R. C. Aster, B. Borchers, and C. H. Thurber, "Linear regression," in *Parameter Estimation and Inverse Problems*, 3rd ed., R. C. Aster, B. Borchers, and C. H. Thurber, Eds., Amsterdam, The Netherlands: Elsevier, 2019, pp. 25–53.
[43] J. A. Tough, D. Blacknell, and S. Quegan, "A statistical description of polarimetric and interferometric synthetic aperture radar data," *Proc. Roy. Soc. London. Ser. A, Math. Phys. Sci.*, vol. 449, no. 1937, pp. 567–589, Jun. 1995, doi: 10.1098/rspa.1995.0059.
[44] R. Touzi, A. Lopes, J. Bruniquel, and P. W. Vachon, "Coherence estimation for SAR imagery," *IEEE Trans. Geosci. Remote Sens.*, vol. 37, no. 1, pp. 135–149, Jan. 1999, doi: 10.1109/36.739146.
[45] C. Albinet et al., "TropiSCAT: A ground based polarimetric scatterometer experiment in tropical forests," *IEEE J. Sel. Topics Appl. Earth Observ. Remote Sens.*, vol. 5, no. 3, pp. 1060–1066, Jun. 2012, doi: 10.1109/JSTARS.2012.2201917.
[46] X. Chen, P. Siqueira, K. McDonald, M. Cosh, A. Colliander, and M. Vanscoy, "L-band radar for forest temporal dynamics," in *Proc. IEEE Int. Geosci. Remote Sens. Symp.*, Pasadena, CA, USA, Jul. 2023, pp. 2637–2640, doi: 10.1109/IGARSS52108.2023.10281944.
[47] Y. Lei, P. Siqueira, and R. Treuhaft, "A physical scattering model of repeat-pass InSAR correlation for vegetation," *Waves Random Complex Media*, vol. 27, no. 1, pp. 129–152, Jan. 2017, doi: 10.1080/17455030.2016.1209594.

Kunyi Chen received the B.S. degree in geographic information science from Peking University, Beijing, China, in 2024, where he is currently pursuing the Ph.D. degree in photogrammetry and remote sensing.

His research interests include interferometric synthetic aperture radar (InSAR), InSAR time-series analysis and decorrelation mechanisms, and the application of InSAR to geoscience and natural hazards response.

Cunren Liang received the B.S. degree from Shandong University of Science and Technology, Qingdao, China, in 2008, and the Ph.D. degree from Peking University, Beijing, China, in 2014.

He is currently an Assistant Professor at Peking University. Previously, he was a Staff Scientist at California Institute of Technology (Caltech), Pasadena, CA, USA, from 2018 to 2021. Prior to Caltech, he was a NASA Postdoctoral Program Fellow at the Jet Propulsion Laboratory (JPL), Pasadena, from 2015 to 2018. His research interests are mainly in the field of microwave remote sensing, e.g., synthetic aperture radar (SAR) signal processing, interferometry (InSAR), microwave scattering mechanisms, and their applications in geosciences.

Dr. Liang is a member of American Geophysical Union. He was a recipient of the NASA Group Achievement Award in 2016 and the JPL Outstanding Postdoctoral Research Award in 2017.

Authorized licensed use limited to: Peking University. Downloaded on August 25,2026 at 14:45:26 UTC from IEEE Xplore. Restrictions apply.